ELSEVIER

International Journal of Mass Spectrometry 203 (2000) 31–47

International Journal of Mass Spectrometry

Simulation-based optimization of the electrodynamic ion funnel for high sensitivity electrospray ionization mass spectrometry

Aleksey V. Tolmachev[a], Taeman Kim[a], Harold R. Udseth[a], Richard D. Smith[a,*], Thomas H. Bailey[b], Jean H. Futrell[b]

[a]*Environmental Molecular Science Laboratory, MS K8-98, Pacific Northwest National Laboratory, P.O. Box 999, Richland, WA 99352, USA*

[b]*Department of Chemistry and Biochemistry, University of Delaware, Newark, DE 19716, USA*

Received 10 April 2000; accepted 7 June 2000

Abstract

High sensitivity is one of the most important requirements for applications of electrospray ionization mass spectrometry (ESI MS). Recent work with the electrodynamic ion funnel has demonstrated that it can provide significantly improved ion transmission through the ESI interface. Here we summarize the results of the simulations for several ion funnel configurations and their comparison with experimental measurements. We also report an alternative treatment of the ion funnel operation based on the effective potential approximation. The analytical relationships derived are used to generalize the results of computer simulations and develop an optimized ion funnel design. The new configuration reduces the spacing between ring electrodes to 1 mm and provides an optimized profile of the ring electrodes radii. It can also generate a deeper effective potential well, resulting in transmission of higher input ion currents over an extended mass range and increased operating pressure range (up to ~20 Torr). Furthermore, light *m/z* ion transmission is improved due to suppression of the effective potential wells near the ion funnel exit. Simulations for an optimized ion funnel configuration indicate unit transmission efficiency in the *m/z* range of interest for most biomolecular research using ESI (approximately *m/z* 100–5000), for 1–5 Torr pressure and ion currents >~1 nA, typical for low flow rate charge-constrained electrosprays (i.e. nanospray). Experimental results obtained with an improved electrodynamic funnel validate the model and demonstrate its general utility for designing rf-damped focusing elements. (Int J Mass Spectrom 203 (2000) 31–47) © 2000 Elsevier Science B.V.

Keywords: Electrospray; Ion cooling; Mass range; Space charge; Computer modeling; Simulation

1. Introduction

Electrospray ionization mass spectrometry (ESI MS) has become an important analytical tool, providing an effective means of analysis ranging from small organic and inorganic compounds to large biomolecules [1–5]. Applications of ESI MS are often limited by the overall sensitivity of the technique and in biological research it is almost axiomatic that increased sensitivity enables new and more effective lines of research. Both ESI sources and interfaces have been improved over the last decade and detection limits are now generally in the femtomole to attomole range [6–10].

A major limitation upon the sensitivity achievable

* Corresponding author.

PII S1387-3806(00)00265-7

with ESI MS is the relatively inefficient transmission of ions in the first differential pumping stage. Here ions formed at atmospheric pressure are transferred into the mass spectrometer via a conductance limit (e.g. capillary, sampling cone, or inlet orifice) to the low-pressure region of the mass analyzer, held at ~0.5–10 Torr [11,12]. Gas-phase collisions and charge–charge repulsion lead to an expansion of the ion cloud and decreased transmission to the lower pressure region. Conventional electrostatic ion optics devices, which effectively focus ions in vacuum, become increasingly ineffective at controlling ion–cloud expansion brought about by gas-phase collisions and repulsive electrostatic forces at pressures greater than 0.01 Torr.

Current ESI MS interfaces utilize collisional focusing multipole ion guides (i.e. quadrupoles, hexapoles, octapoles) utilizing rf electrodynamic fields successfully at pressures up to ~0.3 Torr [13–18]. Recent implementation of the segmented quadrupole rf ion guide followed by a small [0.35 mm inner diameter (i.d.)] skimmer has demonstrated effective collisional focusing at pressures 0.1–3 Torr [19]. However, the effective acceptance aperture of the rf quadrupoles is limited by the radial dimensions, typically <~10 mm.

This laboratory has recently proposed an alternative rf field device for focusing ions using a stack of ring electrodes with approximately equal spacing between the rings [20,21]. In this device, the ion confinement depends on the diameter and the spacing between the ring electrodes as well as the rf frequency and amplitude. These characteristics roughly correspond to rod diameter and spacing in rf multipole devices. Such ring electrode devices have been used far less frequently than conventional ion guides and prior to this work were restricted to use as ion guides at relatively high vacuum. It has also been pointed out that the ring ion guide effectively forms a series of ion traps having shallow pseudopotential wells that may serve as transient traps for ions and decrease ion transmission efficiency [22].

We have implemented a specific configuration of the rf stacked ring ion guide, electrodynamic ion funnel, in the intermediate pressure region (~1–10 Torr) of the ESI MS interface and demonstrated that a substantial improvement of the electrospray ion source efficiency may be achieved [23–25]. The ion funnel consists of a series of ring electrodes with an initial (entry) electrode possessing a large internal diameter for efficient ion acceptance. The internal diameter of each subsequent electrode is progressively reduced to that of a much smaller exit aperture (the final electrode). By co-applying rf fields of alternate phase (180°) on each successive electrode in conjunction with a dc potential gradient, to push ions "down the throat" of the ion funnel, ions can be effectively captured, focused, and transmitted through the device, producing a more intense and collimated ion beam. Previous ion funnel designs have demonstrated nearly 100% ion transmission efficiency through the ion funnel over a limited *m/z* range for biopolymers ions [23–25].

In this work we summarize the results of simulations for different ion funnel configurations. Computer modeling of the ion funnel has been found to reproduce experimental results obtained with the early ion funnel designs [25]. We also report an alternative treatment of the ion funnel operation based on the effective potential approximation. The derived analytical relationships have been used to generalize results of computer simulations and to estimate parameters for a new, optimized ion funnel design. Ion transmission characteristics of the optimized ion funnel configuration obtained from computer simulations are compared to experimental data obtained using the new ion funnel design.

2. Methods

A diagram for an ion funnel interface is given in Fig. 1. The ion funnel shown employs a heated inlet capillary and an rf multipole (e.g. quadrupole) for efficient transmission through the second differential pumping stage to the mass analyzer. Although we illustrate the heated capillary arrangement for ESI, it should be noted that similar considerations would apply for other types of higher pressure ion sources and alternative inlet configurations. Fig. 1(b) gives the notation used to describe important ion funnel param-

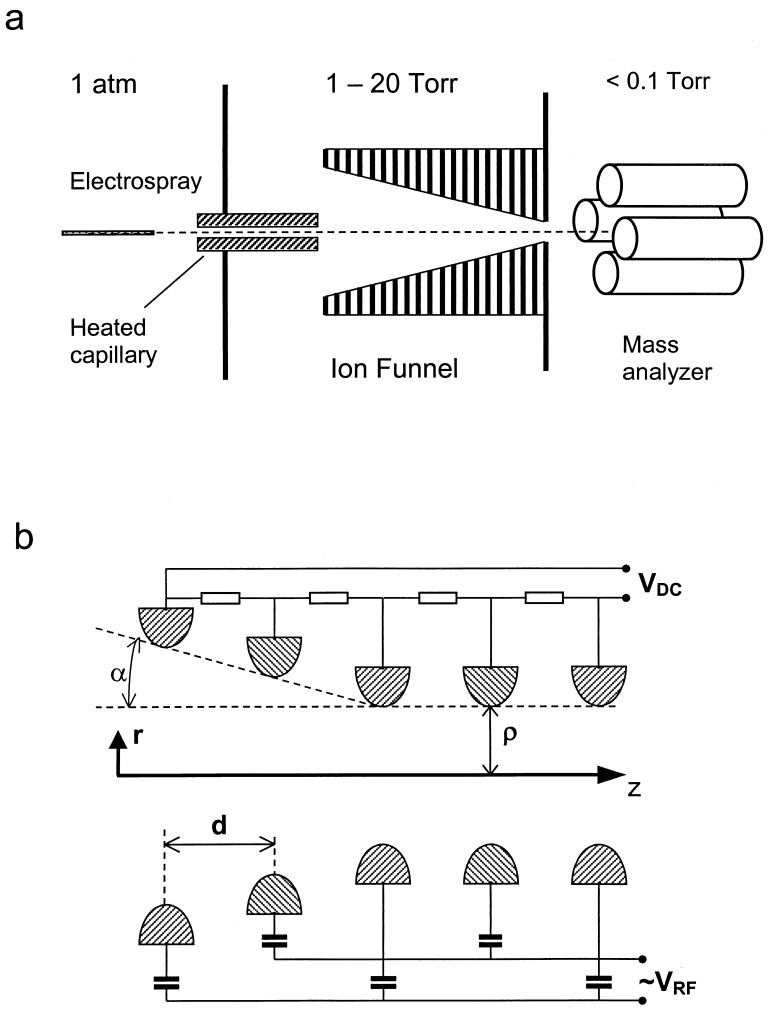

Fig. 1. Schematic diagram of the ion funnel. (a) Atmospheric pressure interface comprising the ion funnel. The ion funnel is installed in the first differential pumping stage. The ESI heated capillary arrangement is shown, although other combinations of the atmospheric pressure ion sources and inlets are possible. (b) The ion funnel schematic indicating notations used in the text: α—angle of the funnel i.d. gradient; d—spacing between ring electrodes; ρ—aperture radius; V_{dc} and V_{rf}—dc and rf voltages applied. The V_{rf} notation is used for the rf voltage amplitude, which is half of the peak-to-peak voltage, $V_{rf} = V_{p\text{-}p}/2$. The cylindrical coordinates r, z are shown.

eters. The V_{rf} notation is used for the rf voltage amplitude, which is half of the peak-to-peak voltage, $V_{rf} = V_{p\text{-}p}/2$. The V_{rf} is commonly used in rf effective potential theory, and we use the value in theoretical relationships and also on plots showing simulation results. Some experimental results, however, use the peak-to-peak voltage $V_{p\text{-}p}$ instead of V_{rf}, and the coefficient 1/2 must be taken into account when comparing the data to theoretical results.

2.1. Ion motion simulations

The computer model developed is similar to the model used previously for collisional focusing in rf-only quadrupole ion guides [16,17], and the one used in a recent treatment of our early ion funnel studies [25]. The model used in this work has been modified to give a more accurate description of the ion-neutral drag and diffusion interactions at ion

velocities higher than the thermal velocity of neutrals. Ion motion is described by the following equation:

$$\frac{d\mathbf{u}}{dt} = -\frac{\mathbf{u}}{\tau} + \mathbf{A}(t) + \frac{q}{m}\mathbf{E}(t) \tag{1}$$

where $\mathbf{u}$ is the ion velocity relative to the local gas flow, τ is the velocity relaxation time, $\mathbf{A}(t)$ is the effective force term resulting from random ion–molecule collisions (mass normalized), q and m are ion charge and mass, and $\mathbf{E}(t)$ is electric field strength, computed as a sum of the fast changing rf and constant dc field components. The first two terms of Eq. (1) correspond to the classical Langevin equation used in the theory of Brownian motion. The random force term $\mathbf{A}(t)$ is required to estimate the radial size of the ion beam resulting from collisional focusing in an inhomogeneous rf electric field [16].

Eq. (1) differs from a simple equation for the ion motion driven by the gas flow and the electric field. The latter equation may be written as $\mathbf{u} = \mathbf{v}_{\text{flow}} + K_E\mathbf{E}$, a sum of local gas flow velocity $\mathbf{v}_{\text{flow}}$ and the electric field induced drift, characterized by a mobility coefficient K_E. Eq. (1) results in a drift motion only after a time interval larger then the relaxation time τ. Thus, Eq. (1) allows one to describe both the vacuum ion motion (for short time intervals, or for low pressures), and the transition to the drift-type motion, typical for high pressure conditions. In addition, the random term $\mathbf{A}(t)$ takes into account ion diffusion. An alternative approach would be to combine the vacuum equation of motion with ion–molecule collision events. However, for a pressure range above 1 Torr the frequency of collisions F_{col} becomes quite high. For a typical biomolecular cross section of 10^{-13} cm^2 [14,15] and 1 Torr pressure $F_{\text{col}} \sim 10^8$ s^{-1}, or ~100 collisions per one period of the rf at 1 MHz. Thus we can replace simulation of separate collisions by adding two terms, one for the drag force, $-\mathbf{u}/\tau$, and one for the random change of the ion velocity, $\mathbf{A}(t)$.

Previously, we used the thermal approximation that is valid when the ion velocity is less than or comparable to the average thermal neutral gas molecule velocity v_{gas} [25]. Here, we explicitly take into account the dependence of the drag force on the ion velocity u. The following relationships were used:

$$\tau = \tau_0 \frac{3/4}{1 + s^2/5}; \qquad s < 1$$

$$\tau = \tau_0\left(s + \frac{2}{3s} - \frac{1}{15s^3}\right)^{-1}; \qquad s \geq 1 \tag{2}$$

$$\tau_0 = \frac{m + m_g}{m_g n \sigma v_{\text{gas}}}; \qquad v_{\text{gas}} = \sqrt{\frac{8kT}{\pi m_g}}$$

where $s = u/v_{\text{gas}}$ is the dimensionless ion velocity, n and m_g are the neutral gas density and molecular mass, σ is the cross section of the ion–molecule collisions, k is the Boltzman constant, and T is the temperature. The relationships (2) were derived for the hard sphere model [16] and were shown to be consistent with other approaches for the drag coefficient estimation [15]. Cross section values, previously measured for several biomolecular ions, were used ($\sigma \sim 10^{-13}$ cm^2 [14,15]).

The random term $\mathbf{A}(t)$ is scaled so that the diffusion coefficient of the ion D corresponds to the ion mobility K_E:

$$K_E = \frac{q}{m}\tau = \frac{q}{kT_D}D \tag{3}$$

Note that the ion mobility dependence on the electric field is taken into account indirectly, through the relaxation time dependence on the ion velocity. The diffusion temperature T_D is used instead of the buffer gas temperature T, to account for the diffusion coefficient increase due to ion motion in an intense electric field. The diffusion temperature may be estimated by averaging of the ΔP^2, where ΔP is the momentum change in a collision; we have used the following approximation:

$$T_D = T + \frac{m_g}{m}\frac{K_{\text{ion}}}{2C_g} \tag{4}$$

where $K_{\text{ion}} = mu^2/2$ is ion kinetic energy, and $C_g = 5k/2$—the heat capacity of a biomolecular buffer gas (e.g. interfaces using dry N_2).

Eq. (1) is used to account for some impacts of gas

flow on ion motion. The effect of the gas flow exiting through the conductance limit (i.e. the orifice immediately following the last element of the ion funnel) was modeled by varying the gas flow centered on the axis behind the orifice at one orifice radius R_{sk} from the orifice plane. The magnitude of the flow is held constant and equal to $\frac{1}{4} n v_c S$ (v_c is the sound velocity, $S = \pi R_{sk}^2$ is the orifice area). This simplified model of exiting gas flow gives an upper estimate for the divergence of ions after the ion funnel exit orifice. Other gas flows of various directions may also be introduced, such as a backward gas flow at the ion funnel inlet or a radial gas flow corresponding to pumping through the space between ring electrodes. The significance of such gas flows increases when rf focusing is weak, and for higher pressures/ion cross section conditions. Results presented here are obtained using only the exiting gas flow; additional flows did not produce a significant influence at the pressure studied. A competition between the drag force imposed on ions by a gas flow, $F_{\text{drag}} = mV_{\text{flow}}/\tau$, and the electric field force qE may be evaluated using the quantity $E_{\text{drag}} = (m/q)(V_{\text{flow}}/\tau)$. In the case of $m/z = 1000$, a gas flow having a supersonic velocity of $V_{\text{flow}} \sim 500$ m/s and $\tau \sim 10^{-6}$ s, typical for pressures ~1 Torr, we obtain $E_{\text{drag}} \sim 50$ V/cm. In other words, it is necessary to apply an electric field of ~50 V/cm to override the supersonic gas flow at a number density corresponding to ~1 Torr pressure. The ion funnel configurations considered here are capable of creating electric fields of such intensity, including both dc and effective rf focusing field. (See Sec. 4 for estimations of the ion funnel effective potential.) We also don't expect the supersonic gas flow to reach the ion funnel ring electrodes, because the Mach disc is positioned only millimeters downstream from the heated capillary exit (0.5-mm i.d.).

The model used in this work disregards effects of the free jet expansion, such as pressure and temperature variations along the free jet. The experimental justification for this assumption is the observation that the ion funnel operation is not sensitive to the heated capillary inlet position along the ion funnel axis [see Fig. 1(a)]. This behavior may be explained similarly to the gas flows considered above. The ion funnel interface design provides a sufficiently large distance between the heated capillary and exit orifice such that main factors defining the ion funnel transmission are space charge repulsion and rf and dc driven ion motion.

The ion motion is computed in three dimensions using a second order integration of the equation of motion (1). The electric field $\mathbf{E}(x, y, z, t)$ is computed as the linear superposition of the dc and rf fields, each computed using a potential relaxation technique [26] for the electrode configuration corresponding to the specific ion funnel design under consideration. Each ion trajectory is followed to the point where it crosses the boundary of a ring electrode (an "ion loss" event), or travels through the exit aperture (a "transmitted ion" event). Ion transmission is defined as the ratio of the transmitted ions to the total number of simulated ion trajectories.

Simulations based upon the first two ion funnel designs [25] have revealed the dependence of ion transmission on the potential wells created at the ion funnel exit, where ring electrode radii ρ are reduced and become comparable with the spacing between ring electrodes, $\rho \sim < d$ [see notation in Fig. 1(b)]. To take into account the increased ion density at the ion funnel exit, it was necessary to create a multiparticle model in which the Coulombic interaction of ions is used to account for space charge effects. Due to computational limitations, the total number of simulated particles was limited to ~1000, so the space charge estimation involved the use of "super ions" in which each ion was assumed to represent a group of ions. The coefficient of the charge multiplication C_{ion} was chosen in accordance with the input ion current considered. The counter charges induced on the ion funnel electrodes were taken into account by introducing a point counter charge located at the center of the rounded boundary of a ring electrode closest to any particular super ion. This crude approximation was primarily used to estimate the importance of the induced charges; in configurations of practical interest, the induced charge effects were found to be negligible.

Each simulation run was conducted to an equilibrium state as follows. The "super ions" initially fill the

simulated region at a rate corresponding to the input ion current. After a short time ions traverse the funnel and the exit ion flow starts to increase. At the moment when the outgoing ion flow equals the input flow an equilibrium state is supposed to be established. The outgoing flow is calculated as the sum of the exit flow and the flow of ions lost on the ion funnel electrodes, as defined above. After the equilibrium state is reached the statistics on the ion transmission and ion density distribution are obtained.

To verify the method stability and to estimate the computational errors due to a coarseness of the time step and the super ion approximation, the equilibrium ion distribution was computed for different time steps and different C_{ion} coefficients. Stable and reproducible results were obtained for time steps of $\sim 10^{-2}$ of one rf period and for C_{ion} coefficients sufficiently small so that the number of super ions per axial distance $\sim d$ is $\gg 1$. Typical time for a simulation run ranges from ~ 1 h to several days using a 300 MHz Pentium II PC.

It is interesting to note that results of simulations showed a weak dependence on the initial conditions, i.e. the coordinates and velocities of ions introduced at the entrance of the simulated region. The "memory" of the initial velocity lasts only ~ 1 μs at a pressure of 1 Torr. For an initial ion velocity of <1000 m/s this corresponds to a path of <1 mm, after which the ion motion becomes independent on the initial velocity and is defined by the local electric field and gas flows. The ion funnel entrance provides sufficient space for both the free jet termination and the collisional relaxation of the initial ion velocity. The ion cloud then expands due to the space charge field and reaches radial positions close to the inner ion funnel surface, where the effective rf focusing balances the space charge repulsion, and a drag from radial gas flows, if present. The most intense competition between these forces occurs at the exit of the ion funnel, where the ion cloud is squeezed to a small radial size. Thus, any major ion losses typically take place at the ion funnel plates near the exit. For this work, detailed simulations of the ion funnel exit were shown to be necessary, and the initial positions of ions proved to be less significant.

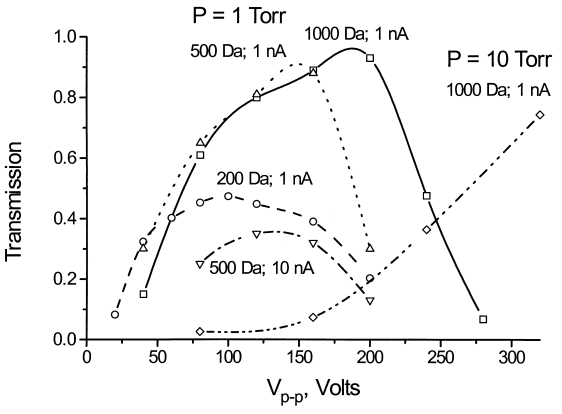

Fig. 2. Simulation for the early ion funnel design #2: $d = 3.2$ mm, exit i.d. = 2 mm. Transmission vs. rf voltage. All curves correspond to $P = 1$ Torr except the diamonds, $P = 10$ Torr. rf = 700 KHz. Ion mass and input current are designated in the plot.

3. Results and discussion

3.1. Simulations of the early ion funnel configurations

The model was first tested by comparing its predictions for the ion funnel designs reported previously [23–25]. Both early designs used 1.6 mm thick ring electrodes separated by 1.6 mm thick insulators, thus the electrode spacing was $d = 3.2$ mm. Twenty-eight ring electrodes were used, their i.d.'s tapered down from 1″ (25.4 mm) at the inlet to 1 mm (design #1) or 2 mm (design #2) ring electrode diameter at the exit of the ion funnel (followed by the 1 mm i.d. conductance limit used in a later implementation). Experimental results have demonstrated that increasing the exit i.d. from 1 mm to 2 mm improved ion transmission, especially at lower *m/z*. The ion motion simulations have shown that ions are accumulated in the effective potential wells created at the center of ring electrodes that have an aperture size close to, or less than the spacing between the rings, $\rho \sim < d$. The *m/z* "window" of transmitted ions for these ion funnel configurations is defined by the competition between different ion species in these effective traps. Increasing the exit ring apertures in the later design decreased the axial wells, resulting in fewer trapped ions and improved transmission over a broader *m/z* range. Fig. 2

summarizes transmission simulations for this configuration for several *m/z*, input current, and pressure values. The results are consistent with the experimental measurements [25].

As seen in Fig. 2, the model predicts ion transmission efficiencies approaching 100% for input currents $<\sim 1$ nA. The optimal parameters (rf voltage and frequency) are *m/z* dependent, and it is not feasible for this design to adjust parameters for uniformly high transmission over a broad *m/z* range. Additionally, ion transmission was limited to $m/z > 200$. The model shows that even with an exit orifice of 2 mm the axial wells are still sufficiently deep to capture ions, resulting in decreased ion transmission. The high *m/z* range was also limited by rf voltage needed to focus the heavy ions. Due to the breakdown limit ($V_{p\text{-}p} < 400$ V) at ~1 Torr pressure, the upper *m/z* efficiently transmitted was $<\sim 2000$. The optimal pressure for this ion funnel configuration is in the range of 1–2 Torr; the simulated ion transmission decreased sharply at pressures <1 Torr and above 5 Torr. The model has shown that at low pressures ions acquire velocities too high to be focused effectively by rf focusing of the stacked ring electrodes. The relationship explaining the behavior is described in Sec. 4.1. The decreased transmission for higher pressures is attributed to the pressure dependence of the effective rf potential discussed in Sec. 4.5.

3.2. The ion funnel configuration with reduced spacing

Simulations have shown that in the practical range of rf frequencies and voltages the axial effective potential wells are quite shallow and ions are not trapped in the section of the ion funnel where apertures have radii larger than electrode spacing $\rho > d$ [25]. Thus improved ion transmission can be expected if the ρ/d ratio of the exit rings is further increased. On the other hand, according to the simulations, major ion losses in design #2 occurred at the 1 mm i.d. conductance limit that followed the last 2 mm i.d. ring electrode of the ion funnel. Increasing the conductance limit aperture may result in excessive pressures downstream of the ion funnel. An alternative solution is to decrease the exit ring apertures down to the conductance limit size while decreasing the spacing between ring electrodes. This approach has been realized in the ion funnel design shown in Fig. 3. The spacing $d = 1$ mm and exit ring i.d. = 1.5 mm has been used, giving a minimum ratio $\rho/d = 0.75$, compared to $\rho/d \approx 0.3$ for the second design, largely eliminating the axial wells. The rings' i.d. gradient chosen for this design was based on a profile illustrated by Fig. 3 (referred to as prototype 3). This shape does not follow from any ion-optical considerations, and was chosen arbitrarily as a starting point for the optimization process. The optimized ion funnel profile is considered later in Sec. 5.

Simulations of the ion funnel configuration with spacing $d = 1$ mm have revealed significantly improved ion transmission properties: for input current up to 10 nA and for $m/z = 500$–2000, unit transmission efficiency was obtained over a wide range of rf voltages. The effective potential is proportional to rf field squared [see Eq. (5) below], thus the 3.2 times closer spacing between ring electrodes resulted in an order of magnitude higher effective potential for the same rf voltage applied. Thus all the limitations related to the effective potential, such as high *m/z* range, the space charge limit on ion current, and maximum operating pressure, are reduced. The configuration operates as an ion guide having a broad *m/z* range, without adjustment of the rf parameters (as needed in the earlier design). This new behavior may be explained as follows: with increased ρ/d ratio, the effective rf potential at the ion funnel exit balances space charge repulsion without resulting in axial ion trapping. Fig. 3 shows a "screen shot" from a simulation demonstrating the efficient focusing of ions, with only minor variations of the ion population along the axis. This aspect of performance is particularly important for interfaces with nonscanning mass spectrometers [e.g. Fourier transform ion cyclotron resonance (FTICR) and time of flight (TOF)].

The improved performance is illustrated by the simulation results in Fig. 4 that show the ion transmission versus rf voltage. One order of magnitude higher input current is transmitted in this configuration. Additionally, the rf voltage needed to reach the

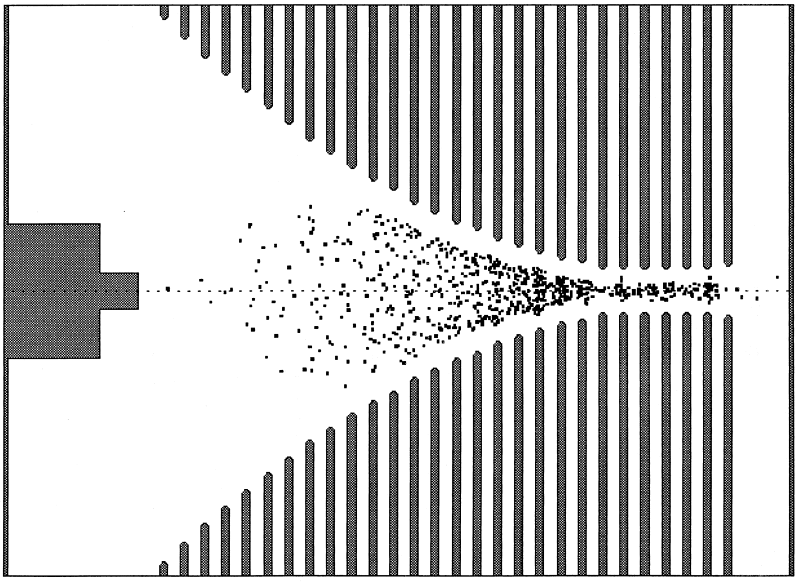

Fig. 3. Simulation for the ion funnel configuration having reduced electrode spacing (d = 1 mm), and the exit orifice i.d. = 1.5 mm; screen capture. Pressure 1 Torr; input current 10 nA; ions m/z = 500 V_{rf} = 35 V; f = 700 KHz. Dots correspond to ions position in projection to (y, z) plane (y—vertical coordinate).

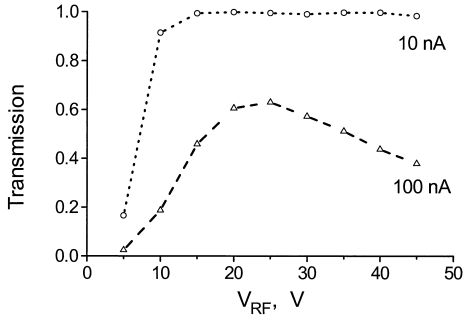

Fig. 4. Simulation results for the ion funnel transmission vs. rf voltage for two input currents: 10 nA and 100 nA. Simulation for the ion funnel configuration having reduced spacing d = 1 mm, and the exit orifice i.d. = 1.5 mm. Pressure 1 Torr; input current 10 nA; ions m/z = 500; f = 700 KHz.

transmission plateau is considerably reduced compared to design #2 (Fig. 2).

Reducing the electrode spacing, d, might be expected to lead to unstable motion of light ions with deterioration of the low m/z cut-off properties of the ion funnel, if one uses an analogy to an rf-only multipole. However, simulations exhibited improved transmission for light ions. For reduced rf voltage/increased rf frequency ions of $m/z \sim 100$ were transmitted efficiently. Evidently the low mass cut off, found experimentally in early designs, resulted from transient trapping in the axial effective potential wells. Thus, suppression of the axial wells with

Table 1
Ion current measurements for 1-mm spacing ion funnel, prototype 3*

Substance	Concentration, μM	Input current, nA	Transmitted current, nA	rf voltage, $V_{p\text{-}p}$, Volts	Transmission, %
Gramicidin S	20	12.5	4.6	13.0	37
Cytohrome C	27	4.3	3.3	26.0	77
Myoglobin	20	14.0	4.4	37.4	31

*Frequency 700 KHz; dc across the funnel 180 V; pressure 1 Torr. Electrospray parameters: needle potential 3.5 KV, flow rate 10 μL/min; heated capillary temperature 150 °C.

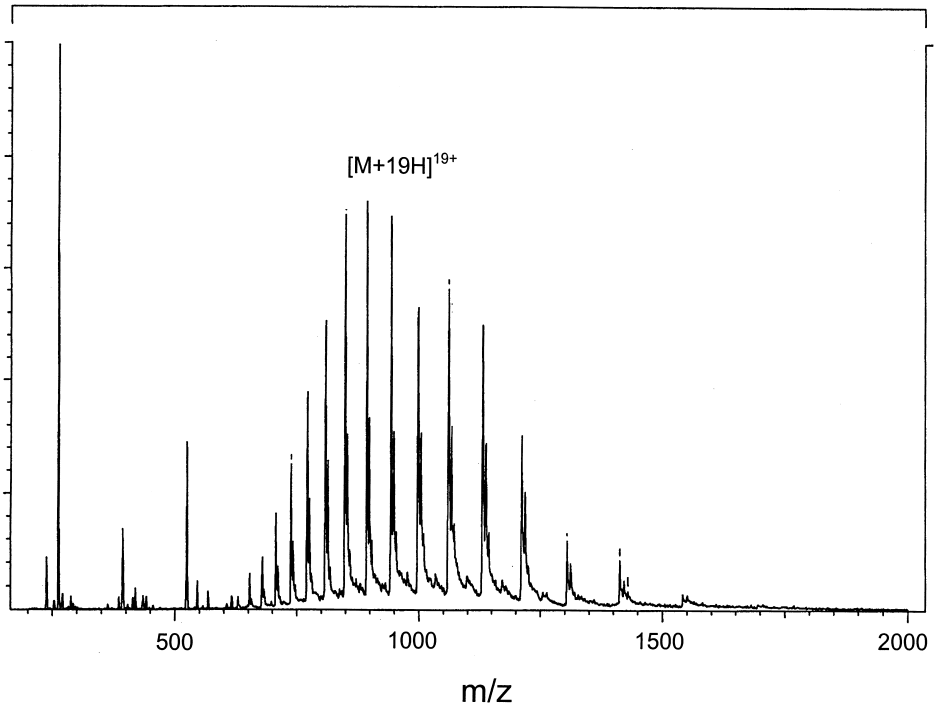

Fig. 5. Spectrum obtained for a 5 μM apomyoglobin solution and a 20 μM L-metethionyl-alginyl-phenylalanyl-alanine acetate solution (MRFA) in 50:50 methanol modified with 0.5% acetic acid. The ion funnel prototype 3 was used in the interface. The ion funnel was operated at 500 kHz, 40 $V_{p\text{-}p}$ rf amplitude and at a pressure of 1.0 Torr.

increased ρ/d is also consistent with the improved transmission for low *m/z* ions.

The experimental evaluation of ion funnel design #3 has confirmed that the new ion funnel design exhibits quite different characteristics compared to the first designs. First, "flat" transmission curves, expected from simulations, have been obtained [27]. According to the model, the flat transmission indicated by the upper curve in Fig. 4 for 10 nA input current shows that ions are focused with an absolute efficiency. Experimental measurements of the dc ion current had demonstrated transmissions up to 70% (Table 1). (It should be noted that the ion current measurements do not allow one to distinguish between the transmission of various *m/z* fractions present in the input current. For example, a fraction of high *m/z* cluster ions not transmitted by the ion funnel would appear to reduce the measured transmission.) The important consequence of the flat transmission is that a wide *m/z* range may be efficiently transmitted through the ion funnel without *m/z*-dependent adjustment of rf parameters. Fig. 5 shows a typical spectrum obtained on the triple quadrupole mass spectrometer TSQ 7000 (Finnigan Mat, San Jose, CA), equipped with the 1-mm ion funnel prototype, using fixed rf parameters: 500 KHz and 40 $V_{p\text{-}p}$. This spectrum shows that the ion funnel configuration can transmit an *m/z* range of 200 to >1500 using a fixed rf amplitude. This expanded *m/z* transmission window with a fixed rf voltage is important for applications in the nonscanning mass spectrometry (such as FTICR). Note that previous ion funnel prototypes required rf voltage to be ramped in order to cover a similar mass range, that is now accessible at a constant and relatively low rf voltage [25].

The rf voltage needed to reach the transmission plateau is also lower for this design, as was expected from the simulation results. As mentioned above,

electrical breakdown limited the maximum rf voltage and resulted in the high *m/z* limit of the previous ion funnel designs. Experiments with the prototype 3 have demonstrated that the considerably lower rf voltage is sufficient to transmit ions over a range of *m/z* 50 to >2000. Fig. 5 demonstrates that *m/z* = 1500 is transmitted at only 40 $V_{p\text{-}p}$, rf 500 KHz, whereas previous configurations used $V_{p\text{-}p}$ = 300 V for optimal transmission [25].

A practical problem encountered with the ion funnel design #3 was that the mechanical assembly and electrical connections were not sufficiently robust, resulting in difficulties in experimental evaluation. A new mechanically improved ion funnel design had been conceived, incorporating further optimization of the ion funnel configuration. However, the computer model, useful in understanding of the ion funnel operation, did not provide a direct way to find the optimal configuration.

4. Analytical relationships

To generalize the results of computer simulations and to facilitate optimization of ion funnel geometry, it was useful to derive analytical relationships giving basic characteristics of the ion funnel. This is done using the effective potential concept [28,21], according to which averaging of the fast rf motion of ions allows one to describe the overall slow motion by the potential

$$V^*(r, z) = \frac{qE_{\mathrm{rf}}^2(r, z)}{4m\omega^2} \tag{5}$$

Here $E_{\mathrm{rf}}(r, z)$ is the absolute value of the local amplitude of rf electric field and $\omega = 2\pi f$ is the angular frequency. The effective potential approximation may be used when the amplitude of the fast rf oscillations is small compared to the characteristic scale of space variations of the field amplitude E_{rf}. If this condition is not met, the ion motion may be unstable and rf focusing is not efficient.

The effective potential at the ion funnel exit is shown in Fig. 6. The potential is calculated on the basis of a numerically computed potential distribution

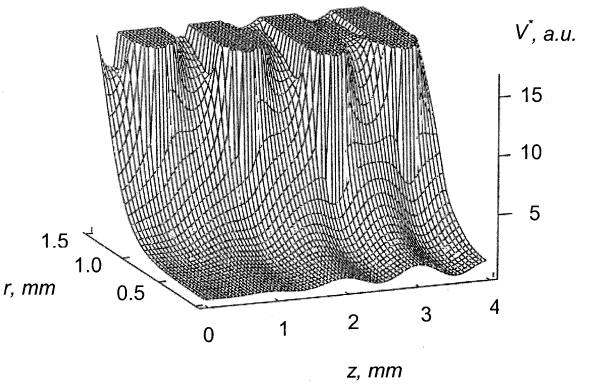

Fig. 6. The effective potential at the ion funnel exit, computed numerically using Eq. (5). Arbitrary units for the potential are used; *r* and *z* are in mm. The cross section of the four exit ring electrodes is shown by equipotential surfaces.

using Eq. (5). The ion motion is confined by the effective potential in the vicinity of the axis, where the effective potential is small. However, at the exit, where the apertures i.d. become comparable to the spacing *d*, axial wells are created. Note that Eq. (5) and Fig. 6 do not account for the dc potential, which may be superimposed on $V^*(r, z)$, to create a driving force toward the ion funnel exit.

To evaluate the effective potential analytically we may use the relationship suggested in [21] for the stacked ring ion guide:

$$V^*(r, z) = V_{\mathrm{trap}}[I_1^2(r/\delta)\cos^2(z/\delta) + I_0^2(r/\delta)\sin^2(z/\delta)] \tag{6}$$

$$V_{\mathrm{trap}} = \frac{V_{\max}}{I_0^2(\rho/\delta)}; \qquad V_{\max} = \frac{qV_{\mathrm{rf}}^2}{4m\omega^2\delta^2} \tag{7}$$

V_{trap} is the axial effective potential well depth; $V_{\max}$ is the maximum value of the effective potential at $r = \rho$, $z = d(i + 1/2)$, $i = 0, 1, \ldots$; I_0, I_1 are zero and first order modified Bessel functions; $\delta = d/\pi$, V_{rf} is the rf voltage amplitude, one half of the peak-to-peak value: $V_{\mathrm{rf}} = V_{p\text{-}p}/2$. The effective potential for a stacked ring ion guide calculated using Eq. (6) is plotted in Fig. 7. The absolute values of V^* in volts were obtained for the following parameters: spacing between the ring electrodes d = 1 mm, ring

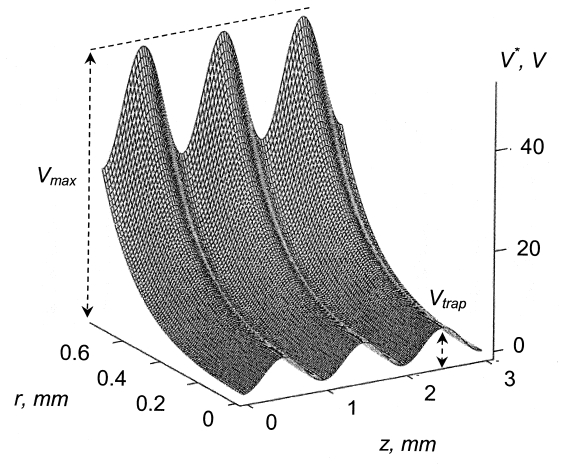

Fig. 7. Effective potential for a stacked ring ion guide, calculated using Eq. (6), Volts. Spacing between the ring electrodes $d = 1$ mm, ring radius $\rho = 0.75$ mm; rf voltage and frequency $V_{rf} = 100$ V, $f = 1$ MHz; $m = 1000$, $q = 1$ e.

radius $\rho = 0.75$ mm; rf voltage and frequency $V_{rf} = 100$ V, $f = 1$ MHz; $m = 1000$, $q = 1$ e.

The relationship (6) does not take into account variable diameters of ring electrodes or the actual shape of the ring electrodes. As a result, the potential from Eq. (6) reaches a maximum value V_{max} between each pair of ring electrodes, whereas the effective potential obtained by direct computation, Fig. 6, is higher at the ring electrode surface at $\rho = r$. This indicates that choosing an optimal thickness and curvature of the ring electrodes can be important for ion funnel performance. Numerical investigation has shown that a smooth effective potential at a radial position approaching ρ is created for ring electrodes having thickness of $d/2$ and the semicircle edge profile; this shape is used as a standard in the modeling described here.

Comparison of the potentials in Figs. 6 and 7 shows that the analytical relationship (6) may be used for rough estimates of characteristic values, such as V_{trap} and V_{max}. Eq. (6) may be simplified using the following approximation for the modified Bessel functions:

$$I_0(x) \approx I_1(x) \approx \frac{\exp(x)}{\sqrt{2\pi x}} \quad \text{for} \quad x \gg 1 \tag{8}$$

After substituting Eq. (8) into Eq. (6) we arrive at the approximation for the effective potential:

$$V^*(r) \approx V_{max} \frac{\rho}{r} \exp\left(\frac{r-\rho}{\delta/2}\right) \quad \text{for} \quad r \gg \delta \tag{9}$$

This approximation neglects the dependence on z, which may be justified for large radii if we are interested in a rough estimate of the effective potential magnitude. We may also use Eq. (9) to estimate the ion density distribution $n(r)$ using the relationship obtained for high space charge/low ion energy conditions [29]:

$$qn(r) = \varepsilon_0 \frac{1}{r} \frac{d}{dr}\left(r \frac{dV^*}{dr}\right) \approx \frac{4\varepsilon_0 V_{max}\rho}{\delta^2 r} \exp\left(\frac{r-\rho}{\delta/2}\right); \quad \delta \ll r < R_q \tag{10}$$

where R_q is the ion cloud radius and ε_0 is the dielectric permittivity constant. It follows from Eq. (10) that the space charge defined ion density distribution in a stacked ring ion guide is concentrated in a thin layer along its boundary, $r = R_q$, with characteristic exponential width of $\delta/2 = d/2\pi$, much less than the spacing between ring electrodes. Relationship (10) is applicable for an ion density high enough so that the distribution width is large compared to the diffusional smearing, estimated in [29] as $\Delta r = 4\lambda_D$, where the Debye length $\lambda_D = (\varepsilon_0 kT/q^2 n)^{1/2}$. This situation is likely to occur when the ion current approaches the space charge limit. In the opposite case of low ion density, the Boltzmann distribution may be used:

$$n(r, z) \propto \exp\left(-\frac{qV^*(r, z)}{kT}\right) \tag{11}$$

Using approximation (8) in Eq. (7) we arrive at a simple relationship for the axial effective potential well depth relative to the maximum effective potential:

$$\frac{V_{trap}}{V_{max}} \approx \frac{2\pi \dfrac{\rho}{\delta}}{\exp\left(\dfrac{2\rho}{\delta}\right)}, \qquad \rho \gg \delta = d/\pi \tag{12}$$

As mentioned above, the ratio V_{trap}/V_{max} must be sufficiently small for efficient operation of the stack of rings at the ion funnel exit. Eq. (12) allows one to estimate the ratio for any spacing and aperture size given. It also explains the large exponential decrease of the axial effective potential wells with increasing ρ/d ratio, obtained from numerical computations.

The stacked ring effective potential, Eq. (6), gives a simple relationship for the effective potential on the axis, at $r = 0$:

$$V^*(0, z) = V_{trap} \sin^2\left(\frac{z}{\delta}\right); \quad (13)$$

$$E^*(0, z) = -\frac{V_{trap}}{\delta} \sin\left(\frac{2z}{\delta}\right)$$

where E^* is the effective field, obtained as the gradient of effective potential, $E^* = -\nabla V^*$. Eq. (13) gives an estimation for the axial dc field E_z, sufficient to override retarding field of the axial wells:

$$E_z > \frac{V_{trap}}{\delta} \quad (14)$$

4.1. Stability conditions

The effective potential approach used above is applicable only if the adiabaticity condition is fulfilled [21]:

$$\eta = \frac{2q|\nabla E_{rf}|}{m\omega^2} \ll 1 \quad (15)$$

Using the Bessel function relationship for E_{rf} [21] and the approximation in Eq. (8) we may estimate the stability parameter as follows:

$$\eta(r) \approx \frac{2qV_{rf}}{m\omega^2\delta^2} \sqrt{\frac{\rho}{r}} \exp\left(\frac{r-\rho}{\delta}\right), \qquad r \gg \delta \quad (16)$$

At the axis:

$$\eta(r = 0) \approx \frac{qV_{rf}}{m\omega^2\delta^2 I_0(\rho/\delta)} \quad (17)$$

Ions having radial kinetic energy K_r oscillate in the effective potential so that the maximum radial position r_{max} is defined by $K_r = qV^*(r_{max})$. Substituting $\eta(r)(16)$ to $V^*(r)$, Eq. (9), we obtain the following limitation: $K_r \ll M\omega^2\delta^2/16$. In terms of the radial component of the ion velocity it can be rewritten as follows: $u_r \ll f \cdot d/\sqrt{2}$. Thus the stacked ring ion guide cannot confine ions above this limit of radial velocity, no matter what rf voltage is applied. A similar limit applies to the z component of the ion velocity: the time interval needed for an ion to travel a distance $\Delta z \sim d$ must be much less than one rf period, $d/u_z \ll 1/f$. We conclude that the ion velocity u must not exceed the limit $u_{max} = d \cdot f$. This relationship is not exact, as is seen from the above derivation. It obviously does not include the case of a static ring electrode guide, for which $f = 0$, but a substantial axial ion velocity is necessary for the ion confinement [30]. However, for the present case of an rf stacked ring electrode guide, the limit on the ion velocity $u < u_{max}$ is a necessary condition for efficient operation.

To test the validity of the relationship, we have performed numerical tests both for the radial and the axial ion velocity limits considered above. Direct simulations of the ion motion in the rf stacked ring ion guide have confirmed that the focusing of ions is less effective for ion velocities approaching or exceeding the u_{max} limit.

We next apply the relationships obtained above to estimate the basic ion transmission characteristics of the ion funnel.

4.2. Low m/z cut off

The limitation $u \ll u_{max} = d \cdot f$ will determine the low *m/z* cut off, especially for low pressure conditions. A low *m/z* cut off also arises from instability in the axial traps, when $\eta(r = 0) > 1$. This situation is more likely to occur at the ion funnel exit where apertures become small, $\rho \sim d$.

4.3. Ion current limit

The maximum ion current transmitted by the stacked ring ion guide may be estimated from the

balance of the space charge repulsion and rf effective focusing [29] as follows:

$$i_{\max} = \pi\varepsilon_0\tau\rho E_z\left(\frac{q}{m}\right)^2 \frac{V_{\mathrm{rf}}^2}{\omega^2\delta^3} \quad (18)$$

To approach the limit $i_{\max}$ the stability condition $\eta \ll 1$ must hold. This relationship explains the improvement in the maximum ion current transmitted by the ion funnel with reduced spacing compared to previous designs (see Fig. 2 and Fig. 4, $i_{\max} \propto 1/d^3$). Decreasing spacing from 3.2 mm to 1 mm results in a factor ~30 increase in the ion current limit. This also explains why the reduced electrode spacing configuration operates at considerably lower rf voltages.

4.4. The high m/z range

For a funnel-shaped stack of rings, the axial dc field E_z is limited by the following inequality:

$$E_z \sin\alpha < E^* < 2V_{\max}/\delta \quad (19)$$

Here the i.d. gradient angle α is defined as follows: $\tan(\alpha) = \Delta\rho/d$, $\Delta\rho$ is the difference of radii of two neighboring apertures [Fig. 1(b)]. Eq. (19) follows from the requirement that the funnel i.d. gradient must be sufficiently small to prevent competition between rf focusing and E_z. The effective field E^* is inversely proportional to *m/z*, hence inequality (19) predicts decreasing transmission for increasing *m/z*.

One additional relationship concerns the ability of the ion funnel to resist the drag force imposed on ions by gas flows: $F_{\mathrm{drag}} = mv_{\mathrm{flow}}/\tau < qE^*$, or $v_{\mathrm{flow}} < K_E E^*$ (v_{flow} = gas flow velocity). This relationship, together with the space charge limit $i_{\max}$, Eq. (18), and the i.d. gradient limit (19), define the high *m/z* range of the ion funnel.

4.5. Pressure limit

The above relationships disregard the decrease of the effective potential due to the buffer gas, which is defined by the coefficient $\gamma = \omega^2\tau^2/(1 + \omega^2\tau^2)$ [16]. This is justified for $\tau \sim 1$ μs, typical for a pressure $p \sim 1$ Torr, and a frequency $f > \sim 1$ MHz. At higher pressures, such that $\omega\tau \ll 1$, $\gamma \rightarrow \omega^2\tau^2$, the rf focusing ability of the ion funnel is decreased: V^*, $E^* \propto 1/p^2$. The limitation on the gas flow becomes $v_{\mathrm{flow}} < \gamma K_E E^* \propto 1/p^3$; maximum current $i_{\max} \propto \tau\gamma E^* \propto 1/p^3$. Thus, taking into account the γ coefficient allows one to estimate the limiting buffer gas pressure for efficient ion funnel operation.

The relationships obtained above should be considered as approximate. The effective potential approximation in Eq. (9) is valid for radial positions larger than the spacing between ring electrodes, and gives only a rough estimate for the ion funnel exit, where $\rho \sim d$. We have also disregarded the effective potential variations at the ion funnel axis due to the funnel-shaped profile. This can be justified by the direct effective potential computation, demonstrating that for the geometry of interest the average effective potential increase due to decreasing radii of rings is small compared to the radial effective potential barrier (Fig. 6). In any case, superposition of the dc potential and the potential surface in Fig. 6 suggests a way to compensate for this trend. Although approximate, the relationships are useful for generalization of computer simulation results and in estimation of optimal ion funnel parameters.

5. An improved ion funnel configuration

The general behavior of the computer model has proved to be consistent with the above relationships based on the effective rf potential concept. The relationships provide an explanation for the improved performance of the 1 mm spacing ion funnel observed both in the computer model and in the experiments (compared to early 3.2 mm spacing designs). Further reduction of electrode spacing may result in decreased transmission due to the limit on ion velocity considered above: $u_{\max} = d \cdot f$. Thus, we have chosen the 1 mm spacing for the implementation of an improved ion funnel configuration. In the new design, the profile of the ion funnel shown in Fig. 3 has been modified: first, a smaller gradient of the ring's i.d. has been implemented in the front part of the ion funnel, and

second, an exit part of a ring's constant i.d. has been removed.

5.1. Smaller gradient of i.d.'s of the ring electrodes

Inequality (19) describes the major limitation on the ion funnel focusing efficiency in the funnel section where rings' i.d.'s are much larger than the spacing between ring electrodes. The dc field necessary to reduce space charge repulsion competes with rf focusing at each ring electrode, and may result in ion loss if the effective field is insufficient (e.g. at high *m/z*), or for excessively high pressure of the buffer gas. Thus, a small gradient of i.d. of the ring electrodes extends the high *m/z* and high pressure ranges of the ion funnel operation. The maximum gradient of $\tan(\alpha) = \Delta\rho/d = 1/4$ was chosen for the new configuration.

5.2. The mechanical alignment accuracy

A radial displacement of a ring electrode position δx creates a local "step" at which rf focusing is weaker and ions may be forced by the dc field to the ring electrode. Using the same considerations as for choosing the i.d. gradient, we arrive at the following condition for the assembly accuracy: $\delta x \ll \Delta\rho \sim d/4 = 0.25$ mm.

5.3. Ion funnel exit configuration

As described above, reduction of the exit diameter is limited by creation of axial ion traps. Optimally, aperture radii should be large compared to spacing: $\rho > d$. An alternative way to reduce the gas load to the next pumping stage is to create a channel of ion funnel ring electrodes having the same relatively small i.d. (Fig. 3 shows such a "stem-like" exit configuration). However, experimental tests of such configurations showed reduced ion transmission, in particular for the low *m/z* ions. The decreased transmission is tentatively attributed to the development of a pressure gradient along the "stem." To verify this assumption the computer simulations have been done for a constant i.d. configuration (for $d = 1$ mm and $\rho = 0.75$ mm) with a linear pressure gradient along the axis. The simulations for $m/z < \sim 200$ have shown that the transmission of such a configuration degrades rapidly for an exit pressure <0.5 Torr. Thus to improve the low *m/z* cut off we have avoided the stem-like exit configuration. The improved ion funnel design implements the constant i.d. gradient of $\tan(\alpha) = \Delta\rho/d = 1/4$, with the last ring electrode i.d. = 1.5 mm. The resulting ion funnel profile is similar to Fig. 1(a).

5.4. Simulation results

Simulations for the new ion funnel design have demonstrated improved ion transmission characteristics. Fig. 8 shows the simulation transmission results for light ions. The transmission of ions $m/z > 50$ is possible. High frequency and larger apertures at the exit facilitate the transmission of light ions. Fig. 9 shows ion funnel transmission simulation results for elevated pressure: 100% transmission is predicted, but increased rf voltage is necessary, $V_{rf} > \sim 100$ V. (It must be stressed that the high pressure operation has not been studied experimentally yet. One may expect deviations of the model used here from a real behavior due to a larger role of gas flows, etc.) For a standard operation mode, $p = 1$–3 Torr, $m/z = 200$–2000, the observed transmission properties are similar to those of the first ion funnel configuration with 1 mm electrode spacing (Figs. 3 and 4). The smaller i.d. gradient used in the optimized configuration results in lower rf voltage sufficient for unit efficiency ion transmission. The high *m/z* range has been improved considerably. Selected simulations have demonstrated a unit transmission of ions $m/z = 5000$ for a practical range of rf parameters and input currents.

5.5. Comparison with experimental measurements

Experimental results for the new ion funnel configuration have recently been reported [31,32]. A Finnigan TSQ 7000 triple quadrupole mass spectrometer modified with the new ion funnel interface was used for these studies. The mechanical design [31,32] allowed precise installation of up to 100 ring electrode

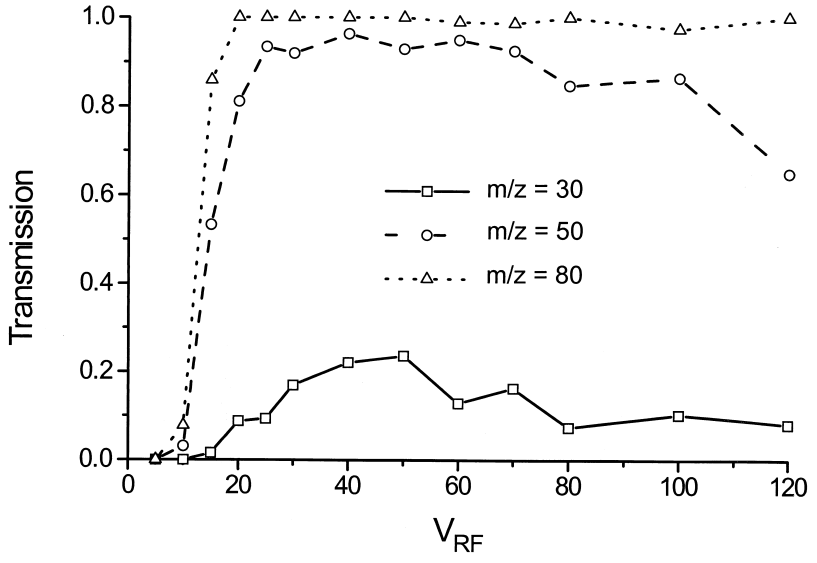

Fig. 8. Light ions transmission vs. RF voltage simulated for the optimized ion funnel configuration. Pressure 1 Torr; input current 1 nA; frequency 3 MHz; DC field E_z = 25 V/cm.

plates of 0.5 mm thickness, spaced by 0.5 mm. The tapered section consisted of 45 rings having conical profile with tan(α) = 0.25, same as in the modeled configuration considered above. An additional 55 rings having constant i.d. = 25.4 mm created the front section of the ion funnel. This 55-mm long cylindrical region was used to adjust the heated capillary position.

The transmission and mass spectra were studied for various biopolymer ions at various pressures, rf amplitudes, and dc potentials. The results confirm the improved transmission properties of the new design. Direct comparison of the experimental data and simulation results are given in Fig. 10. Importantly, no adjustable parameters are used for these simulations. Note the extremely low rf voltages required to reach unit transmission efficiency, $V_{p\text{-}p}$ = 30 V (V_{rf} = 15 V).

The optimized ion funnel configuration has also been recently implemented in a 3.5 tesla ESI FTICR mass spectrometer [33]. This apparatus has more efficient pumping following the ion funnel stage and a larger exit aperture of 2.5 mm i.d. has been used. Initial results again show dramatically improved ion transmission as compared to the conventional capillary-skimmer arrangement. A detection limit of 30 zeptomoles (~18 000 molecules) has been demonstrated for the analysis of proteins with molecular weights ranging from 8 kDa to 20 kDa.

6. Conclusions

A computer model for the ion funnel has been developed and the results of simulations were found

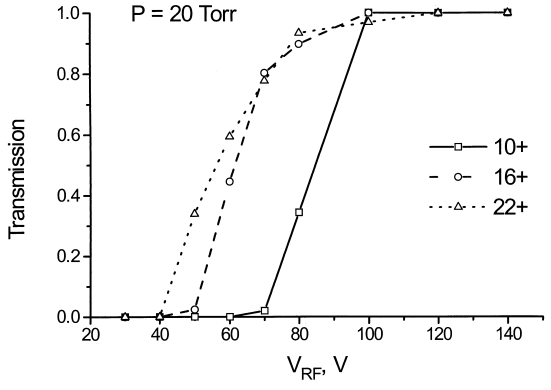

Fig. 9. Transmission for three charge states of myoglobin ions, simulated for the optimized ion funnel configuration. Pressure 20 Torr; input current 10 nA; frequency 1 MHz; dc field E_z = 50 V/cm.

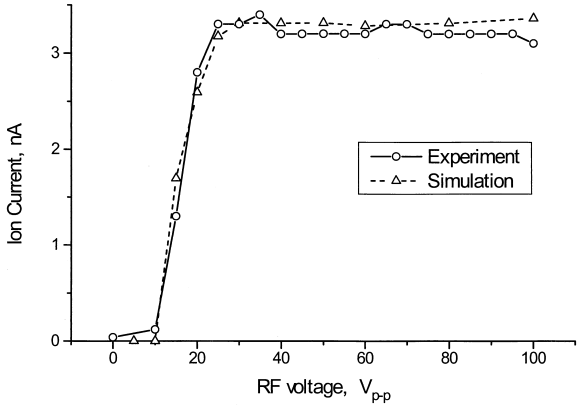

Fig. 10. Transmission of gramicidin ions, comparison of experiment (circles) and simulation (triangles). The ion current has been measured after the ion funnel exit for pressure 1 Torr, input current 5 nA, frequency 0.7 MHz, axial dc field 16 V/cm. Simulations were carried out for the same conditions; the ion current was supposed to consist of equal amounts of 1+ and 2+ gramicidin ions.

consistent with experimental data for several ion funnel designs. Analytical relationships derived on the basis of the effective potential approach provided estimates of the ion transmission characteristics of the ion funnel, such as *m/z* range, ion current upper limit, and effective operating pressure. Based upon these results, a new ion funnel design has been developed. Reduction of the spacing between ring electrodes to 1 mm resulted in suppression of the effective potential wells at the funnel exit, greatly improving ion transmission properties, especially for light ions. It also increased the effective potential of the confinement field, thus providing efficient operation at much higher input currents and pressures, and for ions of higher *m/z*. The gradient of the ring electrodes apertures has also been optimized, resulting in improvements for both low and high *m/z* ion transmission. Simulations for the new ion funnel configuration have shown "flat" 100% transmission versus rf voltage in a wide *m/z* range of ions, for input currents $\sim 10^{-8}$ A. The optimal pressure was found to be 1–5 Torr, but efficient operation has been predicted for up to 20 Torr. These results are expected to guide the development of improved sensitivity mass spectrometers and more effective pumping system arrangements.

Finally, we note that by providing efficient ion transport from the intermediate pressure stage into the next higher vacuum region, the ion funnel also decouples this stage from the atmospheric pressure ion inlet (e.g. a heated capillary or an orifice). We are currently investigating options for further enhancing the atmospheric pressure ion inlet efficiency by using an increased i.d. orifice or the use of multicapillary inlets, followed by the ion funnel [34].

Acknowledgements

Portions of this research were supported by the U.S. Department of Energy, Office of Biological and Environmental Research, and the NIH National Center for Research Resources under Grant RR12365. The Pacific Northwest National Laboratory is operated by Battelle Memorial Institute for the U.S. Department of Energy through contract DE-AC06-76RLO 1830.

References

[1] J.B. Fenn, M. Mann, C.K. Meng, S.F. Wong, C.M. Whitehouse, Science 246 (1989) 64.
[2] J.B. Fenn, M. Mann, C.K. Meng, S.F. Wong, C.M. Whitehouse, Mass Spectrom. Rev. 9 (1990) 37.
[3] R.D. Smith, J.A. Loo, C.G. Edmonds, C.J. Baringa, H.R. Udseth, Anal. Chem. 62 (1990) 882.
[4] R.D. Smith, J.A. Loo, R.R.O. Loo, M. Busman, H.R. Udseth, Mass Spectrom. Rev. 10 (1991) 359.
[5] A.L. Burlingame, R.K. Boyd, S.J. Gaskell, Anal. Chem. 70 (1998) 647R.
[6] J.H. Wahl, D.R. Goodlet, H.R. Udseth, R.D. Smith, Anal. Chem. 64 (1992) 3194.
[7] J.H. Wahl, D.R. Goodlet, H.R. Udseth, R.D. Smith, J. Am. Chem. Soc. 115 (1993) 803.
[8] P.E. Andren, M.R. Emmett, R.M. Caprioli, J. Am. Soc. Mass Spectrom. 5 (1994) 867.
[9] G.A. Valaskovic, N.L. Kelleher, F.W. McLafferty, Science 273 (1996) 1199.
[10] D. Figeys, I. Vanoostveen, A. Ducret, R. Aebersold, Anal. Chem. 68 (1996) 1822.
[11] M. Busman, J. Sunner, C.R. Vogel, J. Am. Soc. Mass Spectrom. 2 (1991) 1.
[12] B.W. Lin, J.J. Sunner, Am. Soc. Mass Spectrom. 5 (1994) 873.
[13] D.J. Douglas, J.B. French, J. Am. Soc. Mass Spectrom. 3 (1992) 398.

[14] T. Covey, D.J. Douglas, J. Am. Soc. Mass Spectrom. 4 (1993) 616.
[15] Y.-L. Chen, B.A. Collings, D.J. Douglas, J. Am. Soc. Mass Spectrom. 8 (1997) 681.
[16] A.V. Tolmachev, I.V. Chernushevich, A.F. Dodonov, K.G. Standing, Nucl. Instrum. Methods Phys. Res. B 124 (1997) 112.
[17] A.V. Tolmachev, I.V. Chernushevich, K.G. Standing, Proceedings of the 45th ASMS Conference on Mass Spectrometry and Allied Topics, Palm Springs, CA, 1997, p. 476.
[18] G. Javahery, B.J. Thomson, Am. Soc. Mass Spectrom. 8 (1997) 697.
[19] A. Dodonov, V. Kozlovsky, A. Loboda, V. Raznikov, I. Sulimenkov, A. Tolmachev, A. Kraft, H. Wollnik, Rapid Commun. Mass Spectrom 11 (1997) 1649.
[20] R. Bahr, D. Gerlich, E.E. Teloy, Verh. Dtsch. Phys. Ges. 4 (1969) 343.
[21] D. Gerlich, in State Selected and State-to State Ion–Molecule Reaction Dynamics. Part 1. Experiment, Vol. LXXXII, C.Y. Ng, M. Baer, (Eds.), Wiley, New York, 1992, pp. 1–176.
[22] J. Franzen, Proceedings of the 44th ASMS Conference on Mass Spectrometry and Allied Topics, Portland, OR, 1996, p. 1170.
[23] S.A. Shaffer, K. Tang, G.A. Anderson, D.C. Prior, H.R. Udseth, R.D. Smith, Rapid Commun. Mass Spectrom. 11 (1997) 1813.
[24] S.A. Shaffer, D.C. Prior, G.A. Anderson, H.R. Udseth, R.D. Smith, Anal. Chem. 70 (1998) 4111.
[25] S.A. Shaffer, A.V. Tolmachev, D.C. Prior, G.A. Anderson, H.R. Udseth, R.D. Smith, Anal. Chem. 71 (1999) 2957.
[26] D.A. Dahl, SIMION 3D Version 6.0, Users' Manual Publication No. INEL-95/0403, Lockheed Idaho Technologies Company, Idaho Falls, ID, 1995.
[27] T. Bailey, J. Futrell, D. Prior, G. Anderson, A. Tolmachev, H. Udesth, R. Smith, Proceedings of the 47th ASMS Conference on Mass Spectrometry and Allied Topics, Dallas, TX, 1999.
[28] H.G. Dehmelt, Adv. At. Mol. Phys. 3 (1967) 53.
[29] A.V. Tolmachev, H.R. Udseth, R.D. Smith, Anal. Chem. 72 (2000) 970.
[30] G. Shenheng, A.G. Marshall, J. Am. Soc. Mass Spectrom. 7 (1996) 101.
[31] T. Kim, A. Tolmachev, D.C. Prior, G. Anderson, H. Udesth, R. Smith, Proceedings of the 47th ASMS Conference on Mass Spectrometry and Allied Topics, Dallas, TX, 1999.
[32] T. Kim, A.V. Tolmachev, R. Harkewicz, D.C. Prior, G. Anderson, H. Udesth, R.D. Smith, T.H. Bailey, V. Rakov, J.H. Futrell, Anal. Chem. 72 (2000) 2247.
[33] M.E. Belov, M.V. Gorshkov, H.R. Udesth, G.A. Anderson, A.V. Tolmachev, D.C. Prior, R. Harkewicz, R.D. Smith, J. Am. Soc. Mass Spectrom. 11 (2000) 19.
[34] T. Kim, H.R. Udseth, R.D. Smith, Anal. Chem., in press.